



HAL
open science

Damage characterization during high temperature fatigue of off-axis woven organic matrix composites for aircraft applications

F. Foti, Y. Pannier, D. Mellier, M. Gigliotti

► To cite this version:

F. Foti, Y. Pannier, D. Mellier, M. Gigliotti. Damage characterization during high temperature fatigue of off-axis woven organic matrix composites for aircraft applications. IOP Conference Series: Materials Science and Engineering, 2018, 13th International Conference on Textile Composites (TEXCOMP-13) 17–19 September 2018, Milan, Italy, 406, pp.012055. 10.1088/1757-899X/406/1/012055. hal-03664787

HAL Id: hal-03664787

<https://hal.science/hal-03664787>

Submitted on 30 May 2022

HAL is a multi-disciplinary open access archive for the deposit and dissemination of scientific research documents, whether they are published or not. The documents may come from teaching and research institutions in France or abroad, or from public or private research centers.

L'archive ouverte pluridisciplinaire **HAL**, est destinée au dépôt et à la diffusion de documents scientifiques de niveau recherche, publiés ou non, émanant des établissements d'enseignement et de recherche français ou étrangers, des laboratoires publics ou privés.

PAPER • OPEN ACCESS

Damage characterization during high temperature fatigue of off-axis woven organic matrix composites for aircraft applications

To cite this article: F. Foti *et al* 2018 *IOP Conf. Ser.: Mater. Sci. Eng.* **406** 012055

View the [article online](#) for updates and enhancements.

You may also like

- [Conductance and Methanol Crossover Investigation of Nafion Membranes in a Vapor-Fed DMFC](#)
Josef Kallo, Wernes Lehnert and Rittmar von Helmlot
- [Effect of carbon nanotubes on the in-plane dynamic behavior of a carbon/epoxy composite under high strain rate compression using SHPB](#)
M Chihi, M Tarfaoui, Y Qureshi *et al.*
- [O₂- and CO-rich Atmospheres for Potentially Habitable Environments on TRAPPIST-1 Planets](#)
Renyu Hu, Luke Peterson and Eric T. Wolf



ECS Membership = Connection

ECS membership connects you to the electrochemical community:

- Facilitate your research and discovery through ECS meetings which convene scientists from around the world;
- Access professional support through your lifetime career;
- Open up mentorship opportunities across the stages of your career;
- Build relationships that nurture partnership, teamwork—and success!

Join ECS!

Visit electrochem.org/join



Damage characterization during high temperature fatigue of off-axis woven organic matrix composites for aircraft applications

F. Foti^{1*}, Y. Pannier¹, D. Mellier¹, M. Gigliotti¹

¹Institut Pprime, University of Poitiers, ISAE-ENSMA, CNRS 3346 - Department of Physics and Mechanics of Materials - 1, Avenue Clément Ader F-86962 Futuroscope Chasseneuil, FRANCE

* federico.foti@ensma.fr

Abstract. The present work focuses on damage characterization during high temperature fatigue of 8HS woven [45]₆ carbon HTS40 carbon fibre/polyimide matrix composite samples. Fatigue tests are performed under controlled environment (air, 2 bar O₂, 2 bar N₂) at 250°C by using a specific experimental setup developed at PPRIME Institute; Digital Image Correlation (DIC) and μ -Computed Tomography (μ CT) are used for monitoring the evolution of sample behaviour during fatigue. It is shown that these two techniques are effective and complementary for damage assessment under fatigue at high temperature under aggressive environment: a rich characterisation of damage extent and orientation can be provided which allows damage being formalised in a way that can be naturally integrated within the context of damage-dependent behaviour models. The employment of such description allows performing full assessment of the effects of environmental fatigue.

1. Introduction

In the next future, the employment of woven organic matrix/carbon fibre composites (OMC) is foreseen for the realization of “warm” structures: these parts may be subjected, in service, to mechanical fatigue (e.g. fan/compressor blades turbo-engines), thermal cycling and thermo-mechanical fatigue (e.g. aircraft structural parts). There is a consistent literature concerning the fatigue behaviour of woven composites [1]–[3] with the use of Digital Image Correlation (DIC, see for instance [4]–[6]) and μ -Computed Tomography (μ CT, see for instance [7]–[9]) for monitoring of damage and degradation phenomena: for satin woven composites under traction-traction fatigue load these studies show that four degradation stages can be identified (see reference [1] for comprehensive review): onset of matrix cracks in the transverse tows subjected to high local bending-induced tensile stress, crack propagation along resin rich regions or towards the longitudinal tow of the same woven ply bringing to meta-delamination, transverse crack propagation and longitudinal tow failure respectively.

Few works are available concerning high-temperature fatigue of textile composites ([10]), while the interaction between fatigue and environmental degradation of has been poorly explored: previous work on environmental fatigue of composite laminates ([11]) has showed that the effect of thermo-oxidation phenomena occurring at high temperature may severely affect fatigue degradation of such materials.

This work aims at characterizing and modelling the high-temperature (250°C) fatigue behaviour of C/polyimide 8HS textile composites, in particular the development of damage related to cyclic mechanical mechanisms (fatigue) under controlled (temperature and gas) environment.



An experimental setup is specifically developed in order to perform fatigue tests under controlled environment (2 bar N₂, air, 2 bar O₂). Sample properties evolution during fatigue tests at 250°C are monitored using in-situ Digital Image Correlation (DIC), and damage assessment is provided by ex-situ X-ray microtomography (μCT). Composite behaviour models are employed for rational understanding of the experimental results.

It is shown that these two techniques are effective and complementary for damage assessment under fatigue at high temperature under aggressive environment: a rich characterisation of damage extent and orientation can be provided which allows damage being formalised in a way that can be naturally integrated within the context of damage-dependent behaviour models. The employment of such description allows performing full assessment of the effects of environmental fatigue.

2. Material, samples, experimental setup and methods

The material is an 8-harness satin [45]₆ woven carbon/polyimide T650-35/MVK-14 composite material produced by Resin Transfer Moulding. The glass transition temperature of the polymer matrix is around 330°C (DMA results), and the matrix volume fraction in the composite is between 34% and 38%: the tow fibre volume fraction is around 60%. The architecture of a unit cell and of the textile composite ply are schematically reported in Fig. 1.

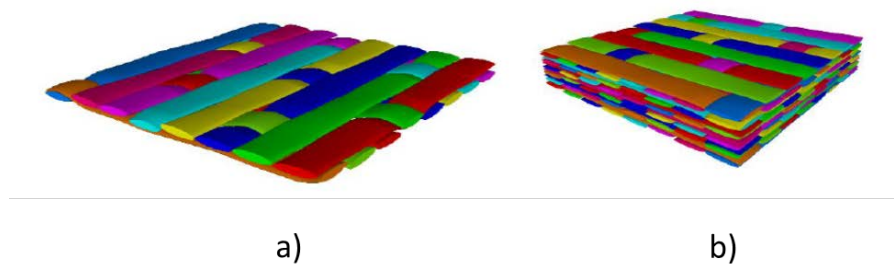


Figure 1. 8 HS woven architecture a) Elementary ply b). Representative Unit Cell. [TexGen®].

All the mechanical tests have been performed using the COMPTINN' test setup illustrated in Figure 2: this is an INSTRON 1251 equipped by a climatic chamber specifically developed to carry out mechanical tests in controlled environment (T_{MAX} : 350°C, p_{MAX} : 5 bar, environment: air, O₂, N₂). The climatic chamber does not allow using gauges for strain measurements, only non-contact techniques can be used for strain measurement.



Figure 2. a) COMPTINN test setup developed @PPRIME b) detail of the climatic chamber.

Tension-tension fatigue tests have been performed under three environmental conditions: air, 2 bar N₂ and 2 bar O₂. Fig. 3 illustrates schematically the load-piloted and the fatigue test: Table 1 presents the fatigue test parameters.

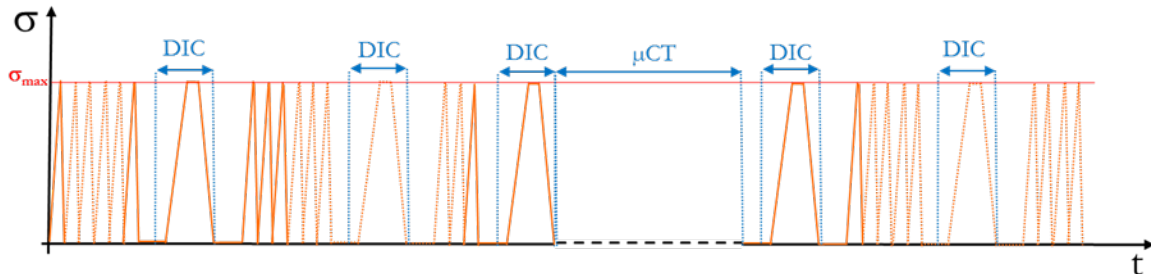


Figure 3. Scheme of the fatigue test with periodic interruption for DIC and μ CT scans.

Table 1. Fatigue test parameters.

Stress Ratio R	Max Stress σ_{MAX} [MPa]	Frequency f (Hz)	Maximum number of cycles	Temperature T [°C]
0.1	75 (~ 55% σ_{FAIL})	2	10^6	250

Fatigue tests were periodically interrupted to carry out intermediate quasi-static load/unload cycles and sample periodically removed from the test rig for μ CT scans.

2.1. Digital Image Correlation (DIC)

For the DIC experimental campaign carried out in this work white particles are directly deposited on the naturally (dark) surface of the composite specimens by using a commercial white spray for use at high temperatures up to 650°C. The average diameter of the particles is 10 ± 7 μ m (measured after the speckle pattern application). During tests, the pictures have been taken using a Nikon D3X camera mounting a Sigma 150mm f/2.8 MACRO zoom. For DIC analysis the CORRELA V.2012 software developed at the PPRIME Institute (see for instance [12]) was employed. The maximal specimen area captured by the camera was 2400×3700 px² (or around 14.5×22.2 mm²) in the central zone of the specimen taking one picture every 6 seconds. A bi-cubic polynomial is selected for the grey levels interpolation inside each subset and the correlations are performed using an iterative algorithm considering also the local displacement gradient. The strain field is calculated from the displacement values using finite difference and the Green-Lagrange tensor [13]. Finally, a low-pass filter is applied on each image to reduce the errors linked to the grey level interpolation. Table 2 summarizes the pixel size, the choice of CORRELA parameters and the errors that could affect the calculated strains. For more details concerning the DIC approach the reader is referred to Reference [13].

Table 2. DIC parameters for fast calculation.

Pixel size	Subset step	Smooth parameter Local gauge length	Correlation error (std)	Environmental error (std)	Max out-of-plane motion error
6-6.2 μ m/mm	40 px	$1/(2 \times 40 \text{ px} \approx 0.5 \text{ mm})$	$\sigma = 2.25 \times 10^{-5}$	$\sigma = 10^{-4}$	5×10^{-5} and 10^{-4} @ $\varepsilon = 1\%$

Max local total error $\approx 2.7 \times 10^{-4}$

A typical strain field observed on the tested woven specimens is reported in Fig. 4a. The output strain field from CORRELA is quite heterogeneous. Several inhomogeneities of the strain field are due to several features, in the present woven architecture the tow width is large enough to contain 4 data points. If some subsets fall on a resin rich region or on a tow or even on a crossover tow, the corresponding

strain value could be different from the surrounding data points lying on the surface tows. Another source of inhomogeneity of the strain field is represented by cracks: since the employed DIC algorithm allows calculating only continuous strain field, cracks appear as large strain regions. To obtain strain values at the macroscopic scale at a given instant of a traction test an arithmetic mean over the whole strain field is calculated. This gives the same results of a virtual extensometer fixed at the upper and bottom sides of the painted region of the specimen.

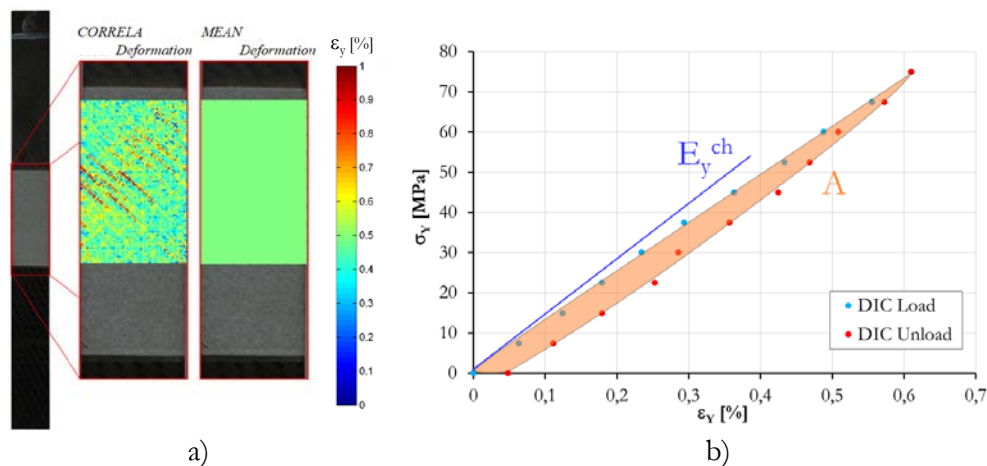


Figure 4. DIC method a) CORRELA output strain field and calculation of mean strain b) stress-strain curve obtained by DIC mean field strain during load-unload traction test.

Fig. 4b. illustrates a typical stress-strain curve obtained by averaging measured DIC strain fields during a traction loading-unloading curve. By this curve it is possible to extract mesoscopic indicators of the material behavior; for instance, the longitudinal chord modulus along the traction direction (y), E_y^{ch} , and the hysteresis area below the whole stress-strain curve, A (Fig. 4b).

DIC can be employed for crack detection by using a separate set of parameters for image correlation, as reported in Table 3.

Table 3. DIC parameters for crack detection.

Pixel size	Subset step	Subset size	Smooth parameter Local gauge length
6-6.2 $\mu\text{m}/\text{mm}$	6 px	6 px	5/(≈ 0.42 mm)

The second part of crack detection is based on image processing. A binary matrix representation of the remaining strain values then analysed by using the Avizo9® software. The binary image is segmented using simple thresholding, a skeletonization is then carried out on the segmentation. By this operation, a line is plotted inside each segmented zone, equidistant to shape boundaries of the element. At the end of this step, the DIC strain field is reduced to a map of segments. Fig. 5 shows the original strain field (Fig. 5a) and the binarization (Fig. 5 b). A MATLAB® script is finally employed to suppress segments oriented along directions different from the expected cracks directions (-45° in Figure 5), hence high strain zones oriented transversally are not considered. The same script is finally employed to measure the length of the remaining segments, reported in blue in Fig. 5c.

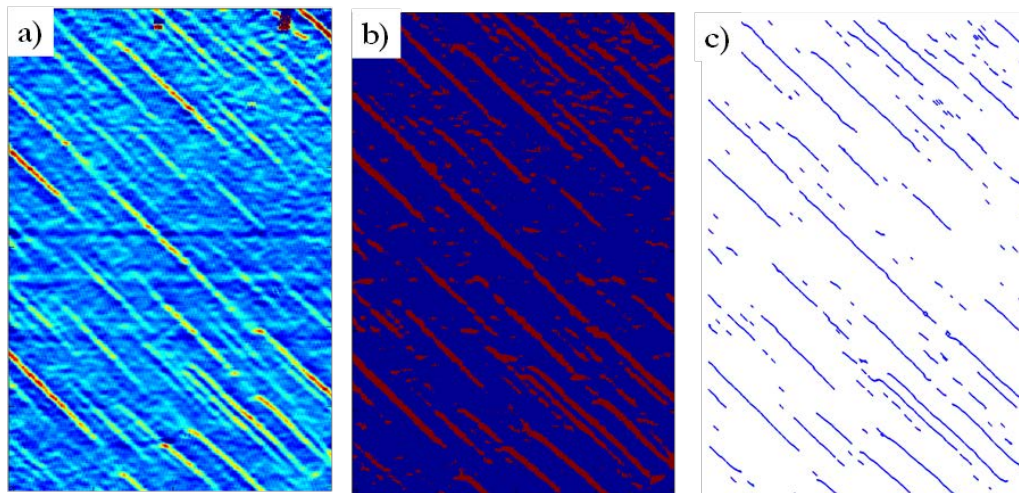


Figure 5. Crack detection by DIC a) original strain field b) binarization c) obtained segments.

2.2. μ -Computed Tomography (μ CT)

μ CT scans are carried out by employing RX Solution UltraTom XL computed tomography system and the 3D images are reconstructed by the X-Act software. The three X-Ray sources mounted on the μ CT system are: a transmission 160 kV nano-focus tube, a reflection 230 kV micro-focus tube and a reflection 150 kV micro-focus tube. For the experimental activity performed in this work, only the last one source has been used. The micro-focus tube Hamamatsu L1216-07 has a maximum power in output of 75 W and an X-ray beam angle of 43° . Between the two available devices for the X-ray detection: a Charge Coupled Device CCD (resolution 4008×2624 px², pixel size $5.9 \mu\text{m}$) and a flat-panel detector Paxscan Varian 2520D (1920×1536 px², pixel size $127 \mu\text{m}$), during the test campaign the Varian detector has been used in agreement with the lower received signal to noise ratio of the Varian detector for the range of used photons energies and flux.

The parameters used for X-Ray generation are reported in Table 4, these parameters are recurrent for this kind of materials. The μ CT scans have been performed using the circular stack acquisition and an anti-ring shift option to reduce ring artifact. The duration of each scan is around 11 hours. The 3D image is obtained using the Filter Back-Projection techniques and using some correction tools. One of this allows correcting beam drift and another one allows correcting the offset in the reconstruction of some slices due to relative oscillations of the specimen respect to the source or the detector. During reconstruction, an anti-ring filter was applied and a reduction of the noise by using the filter back projection reconstruction algorithm was obtained.

Table 4. μ CT parameters.

Voltage [kV]	Current Intensity [μA]	Power [W]	Averaging	Frame Rate	Spatial Resolution [$\mu\text{m}/\text{px}$]
60	139	8.34	20	4.8	8.79

Fig. 6 illustrates a μ CT segmented scan of the external surface ply (exterior ply) of the sample (a non-segmented image is shown in Fig. 6a): Fig. 6b illustrates cracks segmentation; matrix 0° cracks (in red), -45° intra-tow cracks along the -45° tows (in blue), Fig. 6c contains superposition of $+45^\circ$ intra-tow cracks (in green) along the $+45^\circ$ tows. A diffuse pattern of cracks can be noted: 0° matrix cracks are small and concentrated in matrix-rich zone, while intra-tow cracks have the direction of the respective tows. It has been demonstrated by deeper observation that these cracks span the whole tow and have all the same height, which is the height of the tow.

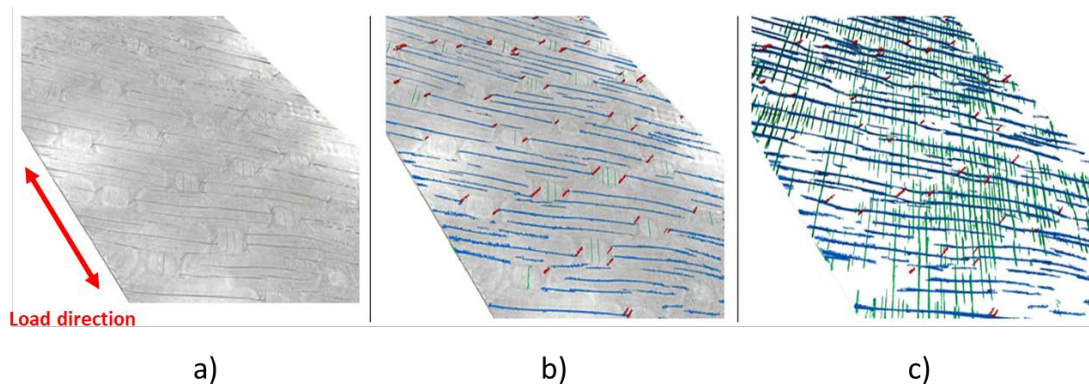


Figure 6. Image resulting from a μ CT scan and segmentation a) non-segmented image b) matrix 0° cracks (in red), -45° intra-tow cracks along the -45° tows (in blue) c) $+45^\circ$ intra-tow cracks (in green) along the $+45^\circ$ tows.

The image processing procedure allows describing crack distribution ply-by-ply and for each tow direction, identifying a stacking sequence of semi-plyes having approximately the thickness of a tow, and in which the cracks have the tow orientation. The total crack length (L) can be used to evaluate the damage level in each semi-ply of the sample (Fig. 7). Figs. 7 illustrates the semi-ply-by-semi-ply crack length distribution as a result of the segmentation procedure for three samples tested at 250°C under different environments (2 bar N_2 , air, 2 bar O_2) for different cycle numbers. The cracks are mainly narrowed on the external semi-plyes (Ply1 -45° and Ply6 $+45^\circ$), while for the inner plies the crack length distribution is quite homogeneous.

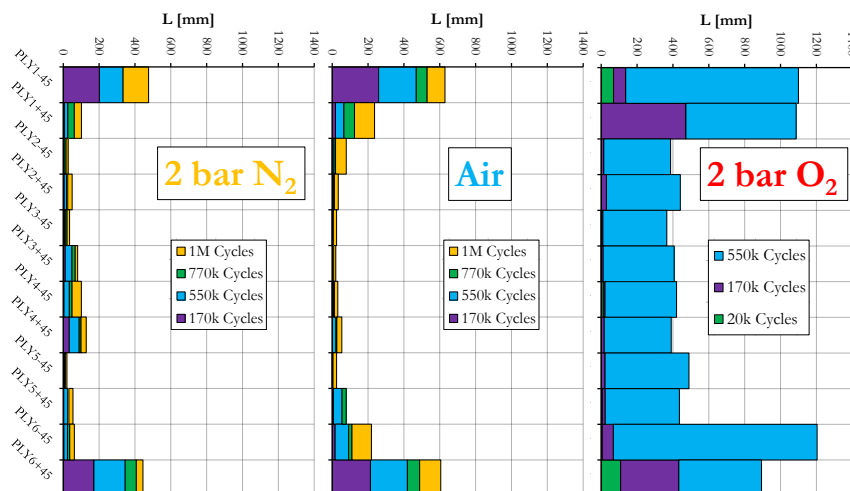


Figure 7. Distribution of crack length along the sample thickness as detected by μ CT scans a) 2 bar N_2 b) Air c) 2 bar O_2 samples.

With respect to the inert environment (2 bar N_2), the effect of thermo-oxidation at high temperature (under air or 2 bar O_2 environment), promotes higher crack density. Crack length is higher in the external plies directly exposed to the environment.

2.3. DIC vs. μ CT crack measurement

Fig. 8a illustrates a superposition of DIC detected cracks (blue) and μ CT scan segmentation results (red) for a sample subject to 770k cycles under air environment. The two measures perfectly match for the most important crack lengths.

A quantitative comparison between the capability of the two techniques for crack detection is illustrated in Figure 24 for Ply1 -45° of a sample subject to 770k cycles under air environment. The graph has two vertical axes: on the left side the crack length values obtained by DIC are reported [L_{DIC}], while the values obtained by the image processing method are shown on the vertical axes on the right [$L_{\mu CT}$]. The scaling factor between the two vertical axes is 2.2 for all the printed point, this is obtained by multiplying the ratio between the analysed area between the crack length evaluation procedures (1.8) and the bias scaling factor previously fixed to 1.23. The two-point series in the graph show a similar trend from the beginning of the test to 1M of cycles.

The DIC crack detection carried out on the tested specimens, allows quickly evaluating the crack length on the external surface of the sample that is the most damaged region of the specimens. DIC crack length results are, thus, exploitable for an evaluation of the damage progression for the whole specimen without removing the specimens from the test rig.

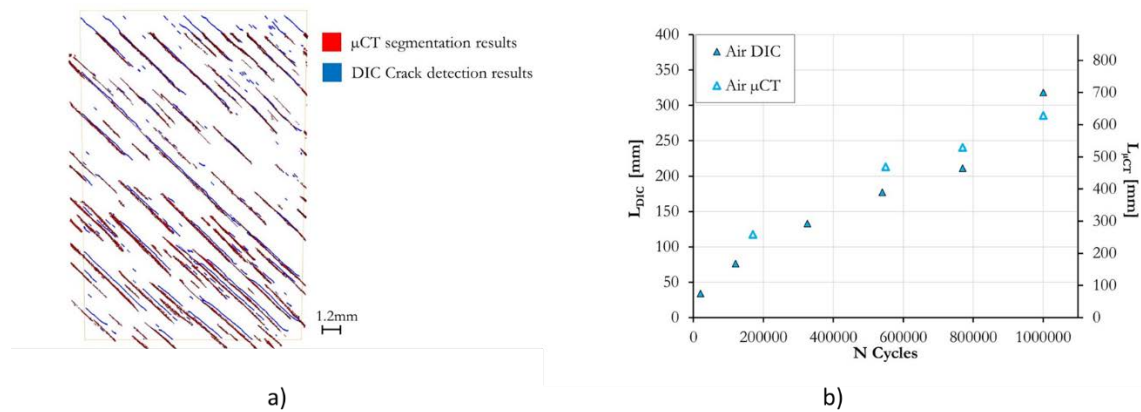


Figure 8. Crack detection and measurement: DIC vs. μ CT a) surface cracks b) evolution of surface crack length as a function of the cycle number.

2.4. Integration of the measured crack system within a laminated damage-dependent mechanical model

The sample architecture (Fig. 1) allows identifying a ply-by-ply discretization, characterized by elementary woven plies with satin texture (Fig. 1a) arranged in a laminated stacked sequence (Fig. 1b).

On the other hand, the volumetric crack distribution revealed by μ CT scans and related segmentation allows identifying a semi-ply-by-semi-ply through-the-thickness crack distribution (Fig. 7), the thickness of a semi-ply being the thickness of a tow which is also the thickness (height) of a crack. Semi-ply is further identified by the orientation or their respective tows which is also the fibre direction and is taken as semi-ply direction 1.

Moreover, μ CT scans (and DIC in the external plies) are able to identify an oriented pattern of microcracks, for each semi-ply (Fig. 6c) with density

$$D_{SP}^{\mu CT} = \frac{L_{SP}^{CRACK}}{L_{SP}} \quad (1)$$

where the subscript SP stands for Semi-Ply, where L_{SP}^{CRACK} is the sum of the crack length (along the tow direction) and L_{SP} is the length of the zone observed by μ CT (around 42.3 mm). Cracks are aligned along the tow direction (semi-ply direction 1) and open along the direction transverse to the tow (semi-ply direction 2): it is therefore plausible to think that they have an effect essentially on the semi-ply

transverse direction (as they directly affect the transverse compliance by crack opening) and the in-plane shear behavior (as cracks may slide with friction in their plane).

It is therefore plausible to construct a semi-ply-based plane stress damage-dependent constitutive law and considering the sample mechanical response as the response of a stacked sequence of damageable semi-ply, having in mind the tows orientation (semi-ply direction = direction 1), the directionality of cracks (along direction 1) and using the lamination theory for constructing the response of the laminate. The damage-dependent constitutive law of the semi-ply is therefore of the form

$$\boldsymbol{\sigma}_{SP} = \mathbf{Q}_{SP}(D)(\boldsymbol{\varepsilon} - \boldsymbol{\varepsilon}_c - \boldsymbol{\varepsilon}_{th}) \quad (2)$$

in which $\boldsymbol{\sigma}_{SP}$ is the semi-ply stress, $\boldsymbol{\varepsilon}$ the total strain, $\boldsymbol{\varepsilon}_c$ and $\boldsymbol{\varepsilon}_{th}$ are, respectively, the inelastic strain related to creep or creep-fatigue interaction and strain of thermal origin (such as those occurring due to material manufacturing at high temperature), $\mathbf{Q}_{SP}(D)$ the semi-ply damage dependent plane stress stiffness matrix given by (in the 1, 2 – tow, transverse-to-tow reference frame)

$$\mathbf{Q}_{SP}(D) = \begin{pmatrix} \frac{E_{11}}{1 - \nu_{12}\nu_{21}} & \frac{\nu_{21}E_{11}}{1 - \nu_{12}\nu_{21}} & 0 \\ \frac{\nu_{21}E_{11}}{1 - \nu_{12}\nu_{21}} & \frac{E_{22}(1 - D_{22})}{1 - \nu_{12}\nu_{21}} & 0 \\ 0 & 0 & G_{12}(1 - D_{12}) \end{pmatrix} \quad (3)$$

in which, for each semi-ply

$$\begin{aligned} D_{22} &= \beta D_{SP}^{\mu CT} \\ D_{12} &= c D_{22} \end{aligned} \quad (4)$$

β and c are interaction parameters. By this way damage acts in a direction perpendicular to that of the tows (D_{22}) and in shear (D_{12}). Following an approach also found in Ref. [14] for satin textile laminates, the stiffness matrix of a ply is given by the algebraic weighted average of the semi-ply: for instance, for the $\pm 45^\circ$ ply one would write

$$\mathbf{Q}_P^{\pm 45} = n_{+45} \mathbf{Q}_{SP}^{+45} + n_{-45} \mathbf{Q}_{SP}^{-45} \quad (5)$$

To each semi-ply is associated an elastic-damage complementary energy density of the form

$$e_{SP}^* = \frac{1}{2} \left[\frac{\sigma_{11}^2}{E_{11}} + \frac{\sigma_{22}^2}{E_{22}(1 - D_{22})} - \frac{2\nu_{12}}{E_{11}} \sigma_{11}\sigma_{22} + \frac{\sigma_{12}^2}{2G_{12}(1 - D_{12})} \right] \quad (6)$$

from which it is possible to calculate by derivation the variables (thermodynamic forces) needed to model the kinetic laws of evolution (which can be improperly referred as energy release rates)

$$\begin{aligned} Y_{22} &= \frac{\partial e_{SP}^*}{\partial D_{22}} = \frac{\sigma_{22}^2}{2E_{22}(1 - D_{22})^2} \\ Y_{12} &= \frac{\partial e_{SP}^*}{\partial D_{12}} = \frac{\sigma_{12}^2}{2G_{12}(1 - D_{12})^2} \end{aligned} \quad (7)$$

3. Mechanical property evolution during high-temperature environmental fatigue

This section focuses on the characterization of material property evolution during high-temperature environmental fatigue and the capability of the damage-dependent modulus of following this evolution,

leaving aside other aspects of the material behavior, such as for instance the evolution of hysteresis area or creep inelastic strain during fatigue.

Figure 9 illustrates the evolution of the longitudinal chord modulus, E_y^{ch} , during fatigue, with increasing the number of cycles. A progressive reduction of the moduli is measured for the three environmental conditions: with respect to the inert environment (2 bar N_2) the kinetic of property decrease is more marked under air and under 2 bar O_2 , oxidizing conditions promote more rapid degradation related to damage evolution (Fig. 7). The laminated semi-ply-by-semi-ply damage-dependent model (dotted lines in Fig. 9) can follow this evolution for a unique value of the parameters β and c , that is, $\beta = 0.035$ and $c = 1$.

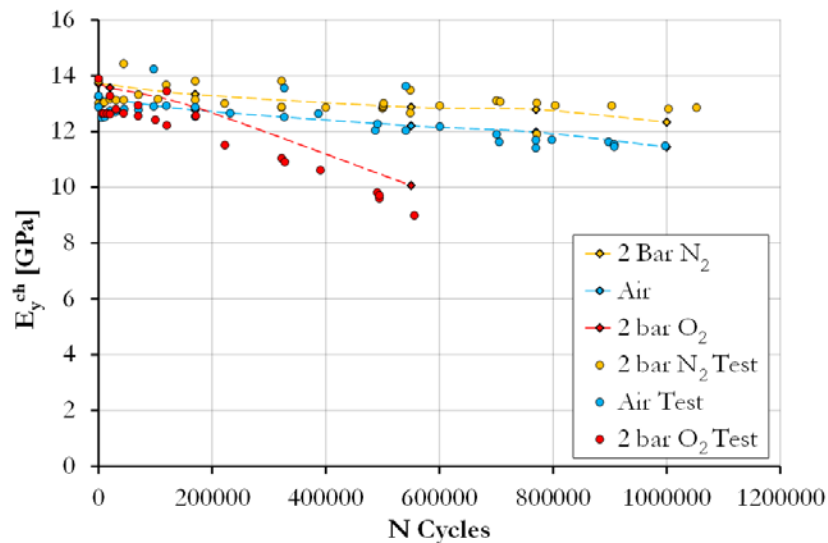


Figure 9. Evolution of the longitudinal chord modulus, E_y^{ch} , during fatigue, with increasing the number of cycles.

Once identified, the model can be employed for the calculation of the thermodynamic forces and to identify the kinetics of damage evolution. For the sake of illustration, Fig. 10 presents the evolution of the thermodynamics forces, Y_{22} and Y_{12} , in the $+45^\circ$ ply, as a function of number of cycles. The thermodynamic forces increase with increasing number of cycles. Moreover, the highest values of Y_{22} and Y_{12} are calculated for the 2 bar O_2 environmental condition.

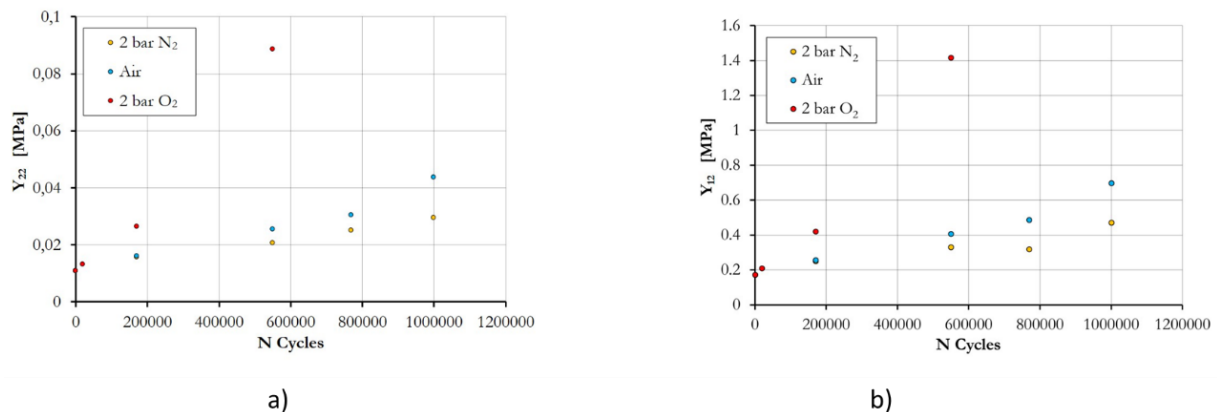


Figure 10. Evolution of the values of the thermodynamics forces, Y_{22} and Y_{12} in the $+45^\circ$ ply as a function of number of cycles.

4. Conclusions and perspectives

This work has been focused on the characterization and modelling of the high-temperature (250°C) fatigue behaviour of C/polyimide 8HS textile composites, the development of damage related to cyclic mechanical mechanisms (fatigue) under controlled (temperature and gas) environment.

An experimental setup is specifically developed in order to perform fatigue tests under controlled environment (2 bar N₂, air, 2 bar O₂). Sample properties evolution during fatigue tests at 250°C are monitored using in-situ Digital Image Correlation (DIC), and damage assessment is provided by ex-situ X-ray microtomography (μCT). It is shown that these two techniques are effective and complementary for damage assessment under fatigue at high temperature under aggressive environment: a rich characterisation of damage extent and orientation can be provided which allows damage being formalised in a way that can be naturally integrated within the context of damage-dependent behaviour models. The employment of such description allows performing full assessment of the effects of environmental fatigue.

Acknowledgements

This work was partially funded by the French Government program "Investissements d'Avenir" (EQUIPEX GAP, reference ANR-11-EQPX-0018). The research subject carried out within this research program falls within the research themes of the French Government program "Investissements d'Avenir" (LABEX INTERACTIFS, reference ANR-11-LABX-0017-01). The authors would like to thank SAFRAN for providing the composite material used in this work. Finally, we acknowledge the Poitou-Charentes Region (France) for funding the PhD Thesis of Federico Foti.

References

- [1] Carvelli V and Lomov SV 2015 *Fatigue of Textile Composites*. Elsevier
- [2] Pandita SD, Huysmans G, Wevers M and Verpoest I 2001 *Composites Part A: Applied Science and Manufacturing* **32** 1533
- [3] Yu B, Blanc R, Soutis C and Withers PJ 2016 *Composites Part A: Applied Science and Manufacturing* **82** 279
- [4] Lomov SV, Ivanov DS, Verpoest I, Zako M, Kurashiki T, Nakai H, Molimard J and Vautrin A 2008 *Composites Part A: Applied Science and Manufacturing* **39** 1218
- [5] Nicoletto G, Anzelotti G and Riva E 2009 *Optics and Lasers in Engineering* **47** 352
- [6] Mehdikhani M, Aravand M, Sabuncuoglu B, Callens MG, Lomov SV and Gorbatikh L 2016 *Composites Structures* **140** 192
- [7] Pazmino J, Carvelli V and Lomov SV 2014 *Composites Part A: Applied Science and Manufacturing* **61** 76
- [8] Barburiski M, Straumit I, Zhang X, Wevers X and Lomov SV 2015 *Composites Part A: Applied Science and Manufacturing* **73** 45
- [9] Sisodia SM, Garcea SC, George AR, Fullwood DT, Spearing SM and Gamstedt EK 2016 *Composites Science and Technology* **131** 12
- [10] Montesano J, Selezneva M, Fawaz Z, Poon C and Behdian K 2012 *Composites Part A: Applied Science and Manufacturing* **43** 1454
- [11] Lafarie-Frenot MC, Rouquié S, Ho NQ and Bellenger V 2006 *Composites Part A: Applied Science and Manufacturing* **37** 662
- [12] Dupré JC, Doumalin P, Husseini HA, Germaneau A and Brémand F 2015 *Strain* **51** 391
- [13] Foti F 2017 PhD Thesis ISAE-ENSMA, Poitiers, France.
- [14] Hochard C and Thollon Y 2010 *International Journal of Fatigue* **32** 1583